Zhong *et al. Soft Sci.* **2025**, *5*, 3
DOI: 10.20517/ss.2024.52

Soft Science

Research Article

Open Access

Check for updates

Calibration-free optical waveguide bending sensor for soft robots

Liang Zhong[1,#], Xiaoqing Tian[2,#], Ji-Yong Wang[3], Jian-Xiang Wang[1], Zhanguo Nie[1], Xueyin Chen[1], Yuxin Peng[1,*]

[1]Institute of Exercise Science and Health Engineering, Zhejiang University, Hangzhou 310058, Zhejiang, China.
[2]School of Mechanical Engineering, Hangzhou Dianzi University, Hangzhou 310018, Zhejiang, China.
[3]School of Electronic and Information, Hangzhou Dianzi University, Hangzhou 310018, Zhejiang, China.
[#]Authors contributed equally.

[*]**Correspondence to:** Prof. Yuxin Peng, Institute of Exercise Science and Health Engineering, Zhejiang University, Yuhangtang Road 866, Hangzhou 310058, Zhejiang, China, E-mail: yxpeng@zju.edu.cn

How to cite this article: Zhong, L.; Tian, X.; Wang, J. Y.; Wang, J. X.; Nie, Z.; Chen, X.; Peng, Y. Calibration-free optical waveguide bending sensor for soft robots. *Soft Sci.* **2025**, *5*, 3. https://dx.doi.org/10.20517/ss.2024.52

Received: 19 Oct 2024 **First Decision:** 27 Nov 2024 **Revised:** 10 Dec 2024 **Accepted:** 17 Dec 2024 **Published:** 16 Jan 2025

Academic Editor: Xing Ma **Copy Editor:** Pei-Yun Wang **Production Editor:** Pei-Yun Wang

Abstract

Soft robots have become increasingly popular due to their compliance, deformability, and adaptability. Soft sensors, particularly bending sensors, play a crucial role in providing essential posture and position information for these robots. However, current soft bending sensors encounter difficulties in accurately measuring joint bending angles and directions under different curvatures. To address these challenges, we propose a novel dual-colored layer structured (DCLS) bending sensor based on the optical soft waveguide. The DCLS sensor is constructed using polydimethylsiloxane (PDMS) as the clear core, with red and blue layers on each side. The sensor's performance is evaluated through experiments involving bending, compression, and impact conditions. The DCLS bending sensor exhibits excellent calibration-free properties, allowing it to effectively monitor bending angles and directions of joints of varying sizes without requiring any additional calibration. The sensor is successfully integrated into various soft robots, including a fruit sorting robot, a fish-inspired robot, and a hand orthotic exoskeleton robot, showcasing its versatility and potential for different applications.

Keywords: Optical waveguide, bending sensor, soft robots, calibration-free

INTRODUCTION

Soft robots are characterized by their compliance, deformability, and adaptability, allowing them to adapt to complex environments and interact safely with humans and delicate objects. Notably, these soft robots have found diverse applications in delicate object interactions[1,2], bionic manipulation[3], assisting in human rehabilitation[4] and surgical procedures[5], *etc.* Correspondingly, soft sensors assume a vital role in facilitating perception for these robots, contributing significantly to their ability to sense and respond to their surroundings. Specifically, soft bending sensors play a key role in detecting attitude changes, providing essential posture and position information[6,7]. Achieving accurate self-shape perception and external environment perception necessitates the seamless integration of soft robots and soft bending sensors[8,9], thereby ushering groundbreaking advancements that enable soft robots to adeptly execute precise and delicate tasks[10-12].

Soft bending sensors can be categorized into two distinct types: non-stretchable bending sensors and stretchable bending sensors. The former is typically fabricated using inextensible substrate materials such as polyimide (PI)[13] and polyethylene terephthalate (PET)[14], which induce significant residual stress during adaptation to bending surfaces. On the other hand, the latter employs deformable substrates such as soft silicone[15,16], leading to reduced residual stress. Both types of bending sensors utilize smart materials as their sensing units, including liquid metal[17-19], soft sensitive polymers[20-22], and piezoelectric material[23-25]. These smart materials respond to the strain on the sensor surface and generate variable electrical properties, such as resistance, conductance, electric charge, and capacitance. Notably, when the same joint is bent, the larger the angle, the greater the change in the electrical signal. However, it is essential to acknowledge that, at a constant degree of bending, the joint with a large radius experiences more substantial deformation to the sensor. This phenomenon necessitates repeated sensor calibration whenever it is mounted on different joints before use[26], posing a common challenge for both commercially available and research-stage soft bending sensors. Furthermore, a notable limitation of most soft bending sensors based on smart materials is their inability to distinguish bending directions[27-29]. This arises from the generation of identical electronic signal responses when the sensor is bent in positive and negative directions. Additionally, the smart materials are sensitive to both pressures and bending, leading to unexpected pressure interference with the bending measurement.

An optical waveguide is a structure that confines and directs light propagation along a predetermined path using total internal reflection, consisting of a core with a higher refractive index than the surrounding cladding or substrate. The soft optical waveguide exhibits remarkable characteristics, including high anti-electromagnetic[30] and excellent extensibility[31], making it well-suited for detecting bending signals and facilitating widespread applications in soft robots and wearable devices[32-39]. In this research, we present a dual-colored layer structured (DCLS) bending sensor based on the soft optical waveguide [Figure 1A, middle]. Red and blue lights are regulated via the dual-colored layers (red and blue). By capitalizing on the light attenuation effect of dual-colored layers, the red and blue output light intensity can be adaptively regulated during the bending process. Consequently, the bending angle can be accurately determined through a light intensity difference algorithm, even for joints of varying sizes. Compared to conventional bending sensors, the DCLS sensor can be directly applied to detect joints of various sizes without requiring calibration, making it, for example, highly suitable for measuring a diverse range of joints in the human body [Figure 1A, left]. Moreover, the variations in the light intensity difference of the DCLS sensor show its capability to measure bi-directional bending angles without recalibration [Figure 1A, right]. Finally, the DCLS sensors are applied in the soft sorting robots for processing agricultural products [Figure 1B, left], fish-inspired robots for exploring the underwater world [Figure 1B, middle], and rehabilitation exoskeleton robots for helping the disabled [Figure 1B, right] to validate their performance and capabilities.

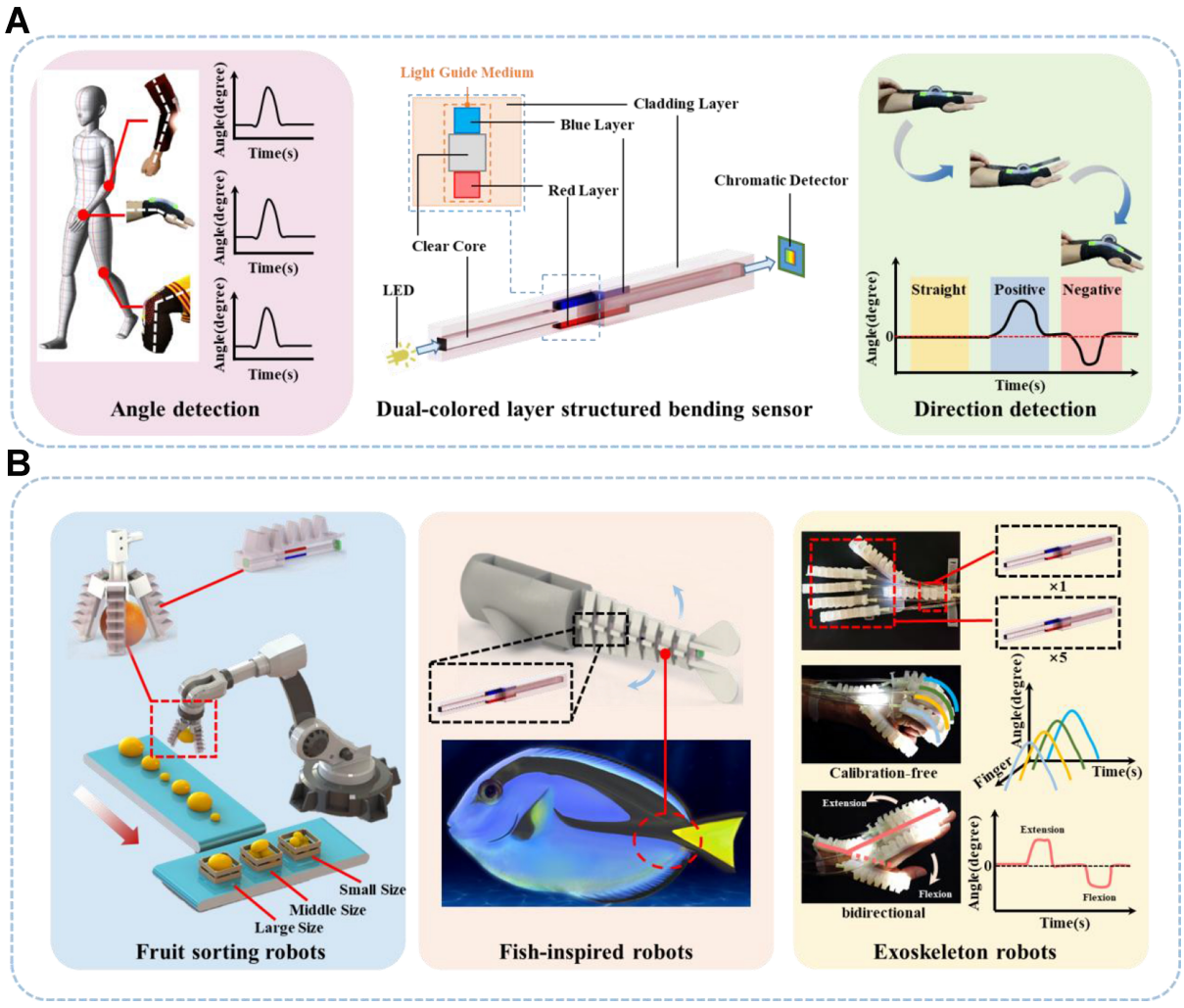

Figure 1. DCLS bending sensor based on soft optical waveguide for various potential applications. (A) Distinctive structure and features of the developed sensor; (B) Potential applications utilizing the DCLS sensor: fruit sorting robots (left), fish-inspired robots (middle) and exoskeleton robots (right). DCLS: Dual-colored layer structured.

METHODS

Preparation of the DCLS sensor

The polydimethylsiloxane (PDMS, Sylgard184, Dow Corning, USA) with a high refractive index ($n \approx 1.41$) was purchased from the market and utilized to fabricate the clear core. The silicone (Ecoflex 00-10, Smooth-On, USA) with a low refractive index ($n \approx 1.40$) was employed as the cladding layer material of the DCLS sensor. A mixture of 30 mL Part A and 30 mL Part B was prepared and stirred uniformly at 25 °C for 3 min. Subsequently, the mixture was poured into the molding. After the silicone was cured, liquid PDMS was mixed with the curing agent at a ratio of 6:1 and stirred at 25 °C for 5 min. Simultaneously, a red colorant (SO-Strong, Smooth-On, USA) was added to the PDMS-curing agent mixture. The mixture was then cured at 80 °C for 12 h. In an analogous manner, the clear core and blue layer were fabricated.

Construction of the experimental setup for characterizing the DCLS sensor

The experimental setup consists of a basement, a stepper, and a swing arm. The basement and the swing arm are fabricated using 3D printing technology (A8s, JG MAKER, China). The stepper is mounted securely to the basement, with its rotating shaft connected to the swing arm. The DSCL sensor is installed within the

swing arm. The stepper drives the swing arm to oscillate through commands sent by the microcontroller.

Construction of the test apparatus for testing accuracy and resolution of the DCLS sensor

The test apparatus was established, comprising a precision stepper (B6-BYGH156), a bending mechanism, and a microcontroller (STM32F103RCT6, STMicroelectronics, Italy). The bending mechanism, manufactured via 3D printing technology (A8s, JG MAKER, China), was designed with interchangeable components to facilitate various bending radii. This feature enables the assessment of the angular measurement accuracy of DCLS sensors across different curvatures. The microcontroller sends pulse signals to the stepper, allowing for highly accurate rotational movements. This test apparatus was also utilized to evaluate the angular resolution of the DCLS sensor.

RESULTS AND DISCUSSION

Working principle of the proposed sensor

As shown in Figure 1A, the DCLS bending sensor is composed of a soft optical waveguide, a light-emitting diode (LED), and a chromatic detector. The waveguide comprises a light guide medium (including a red layer, a blue layer, and a clear core) and a cladding layer. A broadband visible light source (350-770 nm, 5,700 K) is emitted by the LED at one end, coupled into the clear core and then uniformly refracted in the light guide medium. The chromatic detector is located at the other end to sense the modulated light. To let the light totally reflect in the optical waveguide, the light guide medium is fabricated using PDMS possessing a high refractive index ($n \approx 1.41$), while the cladding layer is made of a flexible silicone material exhibiting a lower refractive index ($n \approx 1.40$). According to Snell's law[40], the closer refractive indices of the clear core and cladding, the greater critical angle. Due to the limitations imposed by the material's refractive index, in order to achieve total internal reflection within the light guide medium, it is necessary to minimize the incident angle of the light source as much as possible. Therefore, we use an LED with a slightly larger emission area (> 3.5 mm × 3.5 mm) than the cross-sectional area of the clear core. This allows the light emitted by the LED to enter perpendicularly to the cross-section, achieving the minimum incident angle (detailed information can be found in Supplementary Texts 1 and 2, Supplementary Figures 1 and 2).

In this study, considering the dimensions of most soft robotic manipulators and aiming to adapt to the applications in these scenarios, the design approach for the sensor size in this research is to simulate the existing robotic manipulator dimensions and integrate the optical waveguide structure within it. This integrated design and manufacturing method exhibit high integrability, avoiding the complex assembly steps and assembly errors associated with traditional sensors that need to be assembled onto soft robots. This method also saves space and reduces the size of the soft robot, which is fully applicable to most soft robotic manipulators. Moreover, since the core components of the DCLS sensor include only micro LED lights and on-chip chromatic detectors, it not only has significantly lower manufacturing costs compared to traditional bending sensors but also offers a smaller size advantage. Theoretically, while maintaining existing functionalities, the entire system's size can be reduced to sub-centimeter levels, providing possibilities for developing more finely detailed and microscale soft robots in the future.

The sensing principle of the proposed sensor is illustrated in Figure 2. When the DCLS sensor is in a straight configuration, the input light propagates through the light guide medium via total internal reflection [Figure 2A]. However, when the DCLS sensor undergoes bending along a rotational axis (where R represents the bending radius and d signifies half the thickness of the sensor), disparate stretching occurs across the upper and lower surfaces, as illustrated in Figure 2B. The stretching difference results in distinct optical path lengths within the red and blue layers. The light intensity attenuation follows the Beer-Lambert's law[41]:

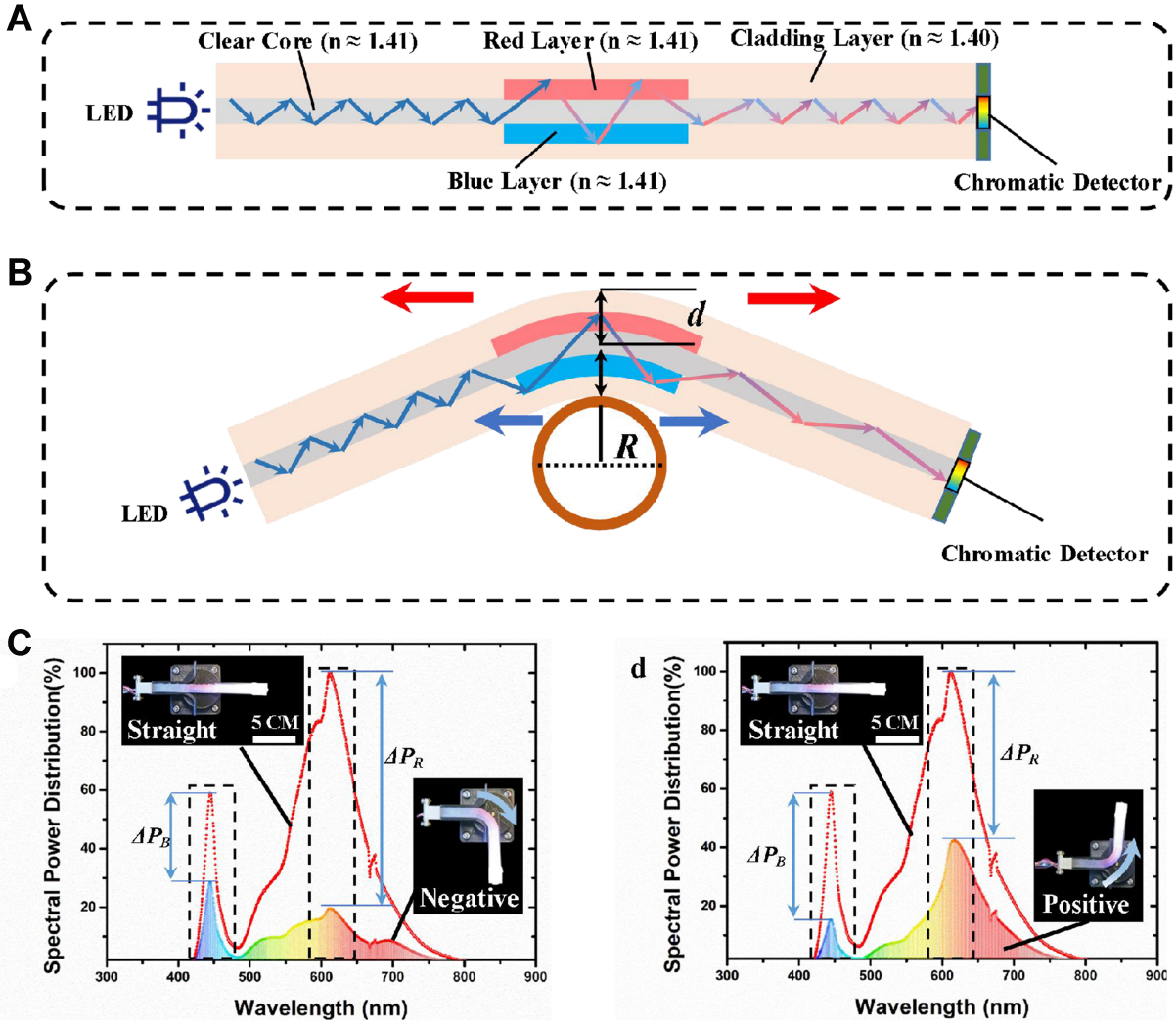

Figure 2. Sensing principle of the DCLS sensor. (A) Inner optical path in the straight state; (B) Inner optical path in the bending state; (C) Spectra of the output light in the straight state (red lines), with clockwise bending (negative bending) (left) and counterclockwise bending (positive bending) (right) by 90°; (D) ΔP_B and ΔP_R indicate the rate of change in integrated power densities for the blue light (440-480 nm) and red light (625-665 nm), respectively. DCLS: Dual-colored layer structured.

$$A = ecl \tag{1}$$

where A is the absorbance of the light absorbance; e and c indicate the molar absorptivity and pigment concentration, respectively. l is the length of either the red or blue layer. Since the absorbance A is proportional to l, the elongation of the upper and lower surfaces of the sensor can be characterized by the light absorbance of the red and blue layers, which results in different colors of the output light and thus can be detected by the chromatic detector.

Figure 2C shows the spectral characteristics of bidirectional bending using the DCLS sensor. A visible light beam is coupled to the soft optical waveguide, the spectrum of which is shown in Figure 2C (red lines) when no bending is applied. It is observed that the power intensity mainly distributes in the blue regime (400-480 nm) and red regime (620-760 nm). Upon clockwise bending of the sensor by 90°, stretching of the red or blue layer induces spectral power variations. Notably, the red layer undergoes greater stretching than the

blue layer, amplifying the attenuation rate (ΔP_R) of the red light, as detailed in Figure 2C (left). Conversely, following the same principle, an anticlockwise bend of the sensor by 90° induces a greater stretch in the blue layer, consequently elevating the attenuation rate (ΔP_B) of the blue light, expounded upon in Figure 2C (right). Thus, the spectral absorption rates of the blue and red light can be quantified as

$$\begin{cases} \Delta P_B = \int_{400nm}^{480nm} s_{straight}(\lambda)d_\lambda - \int_{400nm}^{480nm} s_{bending}(\lambda)d_\lambda \\ \Delta P_R = \int_{620nm}^{760nm} s_{straight}(\lambda)d_\lambda - \int_{620nm}^{760nm} s_{bending}(\lambda)d_\lambda \end{cases} \quad (2)$$

where d_λ is the wavelength of the output light; $S_{straight}$ and $S_{bending}$ indicate the relative energy density in the straight and bending states, respectively. The bending angles and directions of the proposed sensor can be directly obtained by calculating the differences of ΔP_B and ΔP_R when the sensor is bent (detailed information can be found in Supplementary Text 3).

The sensor calculates angles based on the difference in intensity changes between red and blue lights. This difference directly reflects the tensile strain on the upper and lower surfaces of the sensor. Tensile strain differences only occur when the sensor bends, as bending causes differential stretching between the top and bottom surfaces of the sensor. When the sensor undergoes axial stretching, the tensile strain rates on both surfaces are consistent. According to the theoretical model presented in Supplementary Text 3, the bending angle is 0°. Therefore, axial stretching does not affect the sensor. The calibration-free measurement characteristic of the sensor is also based on this principle, as there is always a difference in tensile strain between the upper and lower surfaces when the sensor bends. This difference allows for the direct calculation of the bending angle using the theoretical model. Compared to traditional bending sensors, this eliminates the need for a calibration process.

Characterization results of the proposed sensor

To characterize the DCLS sensor, a specialized experimental setup comprising a basement, a stepper, and a swing arm is used for performance assessment [Supplementary Figure 3]. The experimental setup has a bending radius of 15 mm. The swing arm, driven by the stepper, imparts lateral bending to the DCLS sensor in both clockwise and counterclockwise directions. We first investigated the relationship between the chromatic intensity difference ($\Delta S = \Delta P_R - \Delta P_B$) and the negative bending angle with a bending radius of 15 mm. The absorbance of the red and blue lights is described in Figure 3A. During the bending process from -90° to +90°, there is a significant difference in the rate of change of light intensity between red and blue lights. This is because when bending from -90° to 0°, the red layer undergoes less stretching than the blue layer, resulting in a longer optical path for blue light in the blue layer, leading to a higher rate of change in the intensity of blue light compared to red light. Conversely, during the bending from 0° to 90°, the red layer experiences greater stretching, resulting in a longer optical path for red light in the red layer, which causes the rate of change in the intensity of red light to be higher than that of blue light.

To assess the signal hysteresis of the sensor under large-angle bending (0°-80°) that simulates practical applications, the sensor was fixed in the same position and underwent repetitive cycles of bending, ranging from 0° to 80°, conducted across 100 cycles. The bending radius of the sensor is also 15 mm. As shown in Figure 3B, the hysteretic coefficients ($E = \Delta m/y_S$, where Δm and y_S represent the maximum hysteresis error and scale, respectively) at the 1st, 50th and 100th cycles are all below 0.1%. This indicates the remarkable restorative capacity of the DCLS sensor, even when subjected to a broad spectrum of bending.

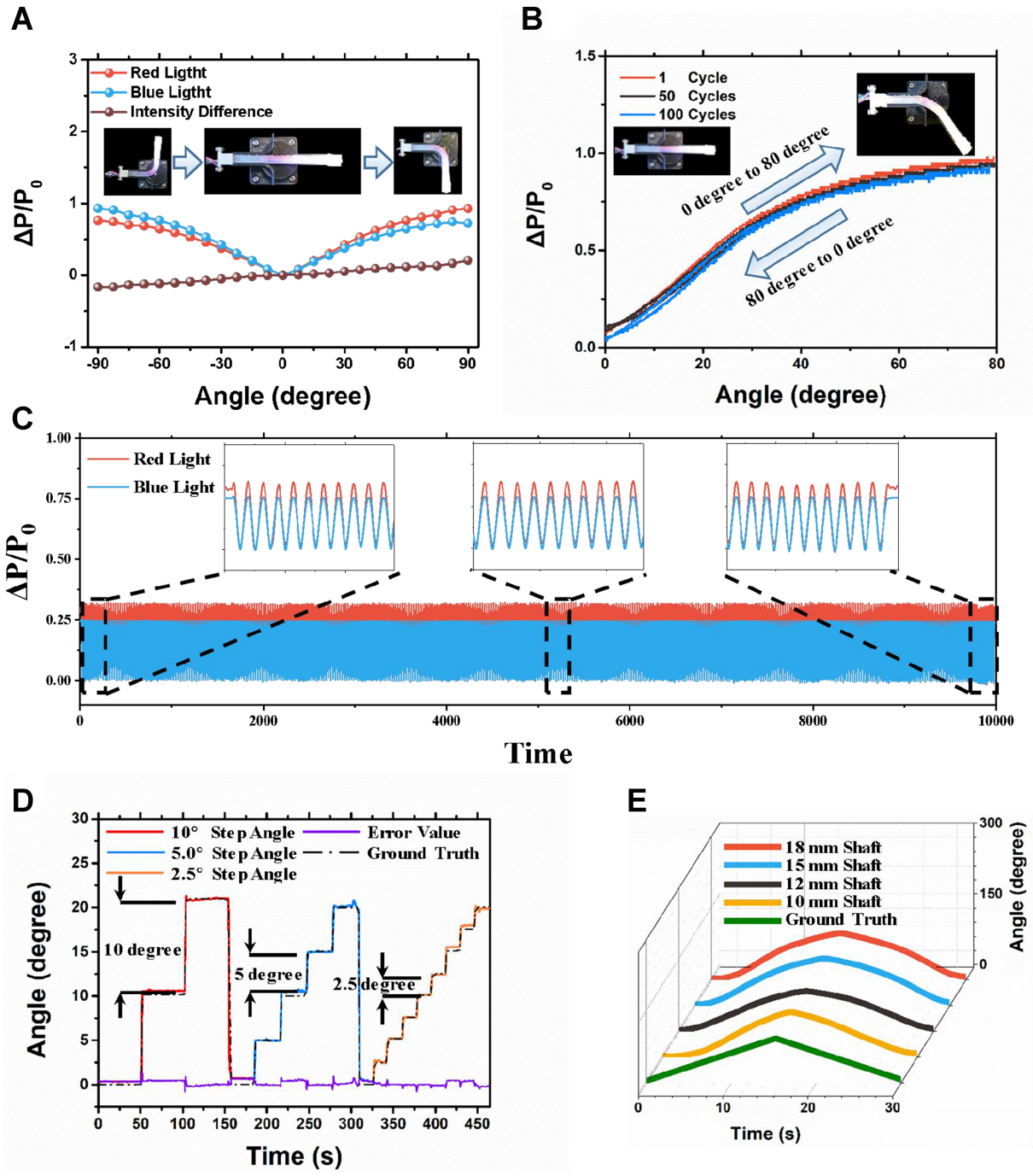

Figure 3. Characterizations of the DCLS sensor. (A) Absorbance as a function of bending angles for the red and blue layers; (B) Absorbance hysteresis of the red layer in different bending cycles; (C) Absorbance tests for 1,000 dual-direction bending cycles; (D) Angle sensing resolution of the DCLS sensor under three different step levels; (E) Bending angles under different bending curvatures. DCLS: Dual-colored layer structured.

Since small-angle bending (0°-45°) is more common in practical applications of the sensor, it is necessary to demonstrate stability during such bending. Therefore, to evaluate the durability of the proposed sensor, we conducted nearly 1,000 bending tests on the sensor using a specialized experimental setup [Supplementary Figure 4]. The bending radius of the sensor was fixed at 15 mm, with the bending angle gradually increasing

from 0° to 30° and then returning to 0°. We recorded the signal response throughout this process to ensure the accuracy and reliability of the data. Figure 3C shows the testing results at a time range of 10,000 s. The insets offer detailed views of the signal within the initial, intermediate, and concluding ten cycles. As can be seen, both the red and blue light signals exhibit stability and maintain near-synchrony. The root-mean-square errors (RMSEs) calculated for the red and blue lights during the initial ten cycles and the concluding ten cycles demonstrate values of 1.26% (red light) and 1.37% (blue light), respectively.

The resolution of the proposed sensor underwent further testing. The sensor was securely affixed to the bending mechanism (with a rotation radius of 15 mm) using adhesive tape [Supplementary Figure 4]. The operation of the stepper motor was controlled by pulse signals generated by a microcontroller, with each pulse causing the motor to rotate by 0.5°. The step angles of the stepper motor were set by varying the frequency of these pulse signals. The stepper motor induced incremental rotations at step angles of 10°, 5°, and 2.5°, respectively, and the stepwise signals of the corresponding sensor were observed. Consequently, the sensor's limit resolution can reach up to 2.5°, as shown in Figure 3D. The negligible deviation observed between the measured angle and the established ground truth confirms the high precision of the proposed sensor.

To validate the accuracy of the bending angle without calibration, the DCLS sensor underwent bending around rotation axes with radii of 10, 12, 15, and 18 mm, respectively. The bending radius of the sensor is the same as the rotating shaft radius of the test apparatus. The sensor underwent a 90° rotation by the test apparatus. As depicted in Figure 3E, the DCLS sensor demonstrates consistent and reliable angle measurements even when adapting to varying bending radii. To verify the universal application of the DCLS sensor in different joints without calibration, a comparative experiment of three types of bending sensors was conducted, including a non-stretchable sensor, a stretchable sensor, and the DCLS sensor [Supplementary Movies 1 and 2]. The study evaluated their performance in measuring the bending angles of wrist, elbow, and knee joints by employing distinct joint protective equipment tailored to each sensor type (detailed information can be found in Supplementary Texts 4 and 5). Participants were instructed to wear the equipment and bend their joints from a neutral state to a bending state of 30°. With only a single calibration, the traditional non-stretchable bending sensor exhibited measurement errors of 5.2%, 22.8%, and 43.3% for the wrist, elbow, and knee joints, respectively [Supplementary Figure 5A]. Meanwhile, the stretchable bending sensor demonstrated measurement errors of 1.3%, 33.3%, and 183.3%, respectively [Supplementary Figure 5B]. In contrast, the DCLS sensor recorded errors of less than 2% when measuring the bending angles of the three distinct joints [Supplementary Figure 5C], demonstrating its superior calibration-free characteristics and adaptability across diverse joint configurations. A comparison of the experimental results of the three sensors can be found in Supplementary Figure 5D and Supplementary Table 1. Moreover, Supplementary Table 2 also provides a comparison of the performance between conventional optical waveguide-based bending sensors and DCLS sensor. More details can be found in Supplementary Figures 6-8.

Finally, additional tests were conducted to evaluate the sensitivity of the DCLS sensor to impact and temperature, and its tolerance to mechanical stress. The DCLS sensor was mounted on a fixed basement and subjected to strikes of 40, 80, and 120 kPa via strike rod. The signal response of the sensor was observed to fall within the range of [0.0, 0.05]. Furthermore, the signal response under impact was compared among the proposed sensor and traditional flexible bending sensors [Supplementary Text 5, Supplementary Figure 9]. To further examine the pressure limit of the sensor, the sensor was mounted beneath a standard force sensor (DY-920, DAYSENSOR, China), and pressure was applied starting from 0 to 1,000 kPa. The experimental findings have ascertained that the withstand pressure level of the DCLS sensor, within its

measurement range, is 1.6 × 10^{-5} dB/kPa. The results demonstrated that the maximum pressure level for the sensor was determined to be 275 kPa [Supplementary Figure 10A, Supplementary Movie 3]. During impact tests, we found that the DCLS sensor exhibits high insensitivity to external mechanical stress, indicating its ability to withstand potential collisions or impacts during use.

To evaluate the temperature drift characteristics of the DCLS sensor, we placed the sensor in a constant temperature chamber for testing. During the experiment, the temperature was increased by 5 °C every 30 min, and the changes in light intensity of red and blue light were recorded in detail. The experimental results show that the temperature drift trends of red and blue lights are highly consistent. Through linear fitting analysis, it is found that the change rates of red and blue light intensity are 0.0141/°C and 0.0142/°C [Supplementary Figure 10B]. This study conducted a series of experiments and data analyses on the performance of the DCLS sensor, revealing its exceptional stability and durability. However, there are some issues that need attention. For example, as the ambient temperature increases, the attenuation of red and blue lights in the light guide medium slightly intensifies. This phenomenon may be attributed to the characteristics of the flexible materials used - as the temperature rises, the difference in refractive index between the cladding and the light guide medium decreases, causing more light to leak out. To address this, future research could consider using light guide medium with higher refractive indices, such as polyurethane, and black silicone with lower refractive indices to further reduce the impact of temperature variations.

DCLS sensor for soft robotic applications

Currently, there are few flexible sensors that are calibration-free. Therefore, we fabricated three distinct types of soft robots: a fruit sorting robot, a fish-inspired robot, and a hand orthotic exoskeleton robot, which were integrated with the DCLS sensor to demonstrate this characteristic. The study protocol was approved by the Medical Ethics Committee from the Department of Psychology and Behavioral Sciences, Zhejiang University, China (reference number: [2022]098), and informed consent was obtained from all participants.

Automatic fruit classification robots play a crucial role in agriculture by enhancing sorting efficiency and significantly reducing labor costs[42]. As illustrated in Figure 4A, we designed a pneumatic grasping robot equipped with the DCLS sensor to grasp target fruits. The details of the design and fabrication can be found in Supplementary Text 6 and Supplementary Figure 11. The robot comprises three pneumatic networks (pneu-nets) actuators, each housing an airway and seamlessly integrating a DCLS sensor. The upper segment of the pneu-nets actuator serves as an air chamber, while the lower section is sealed with a DCLS sensor through an integrated casting method. The pneu-nets actuators can conform to the external fruit surface when bent, facilitating efficient manipulation. Upon installation of the DCLS sensor on the robot, recalibration is not required to detect the external surface curvatures of the robot's pneu-nets actuator. This capability assists the soft robot in discerning fruit sizes, thereby enabling rapid sorting decisions. Figure 4B illustrates the sorting process of such a soft robot. Notably, the absorbance difference between the red and blue layers exhibits an almost linear correlation with the curvature of fruit surfaces, inversely proportional to the size of ordinary oranges. According to the curvature measured by the DCLS sensors, the fruit size can be promptly recognized and then sorted using a threshold judgment [Supplementary Movie 4].

The fish-inspired robot serves as a pivotal tool in deep-sea exploration[43,44]. Accurate detection of the tail's swing angle is imperative for precise control of this robot. As shown in Figure 5A, a fish-inspired robot featuring multiple spines was crafted, incorporating the seamless integration of a DCLS sensor within these structural elements. The details of the design and fabrication can be found in Supplementary Text 6. Within the fish body, provisions were made to securely house essential components such as the battery, servo

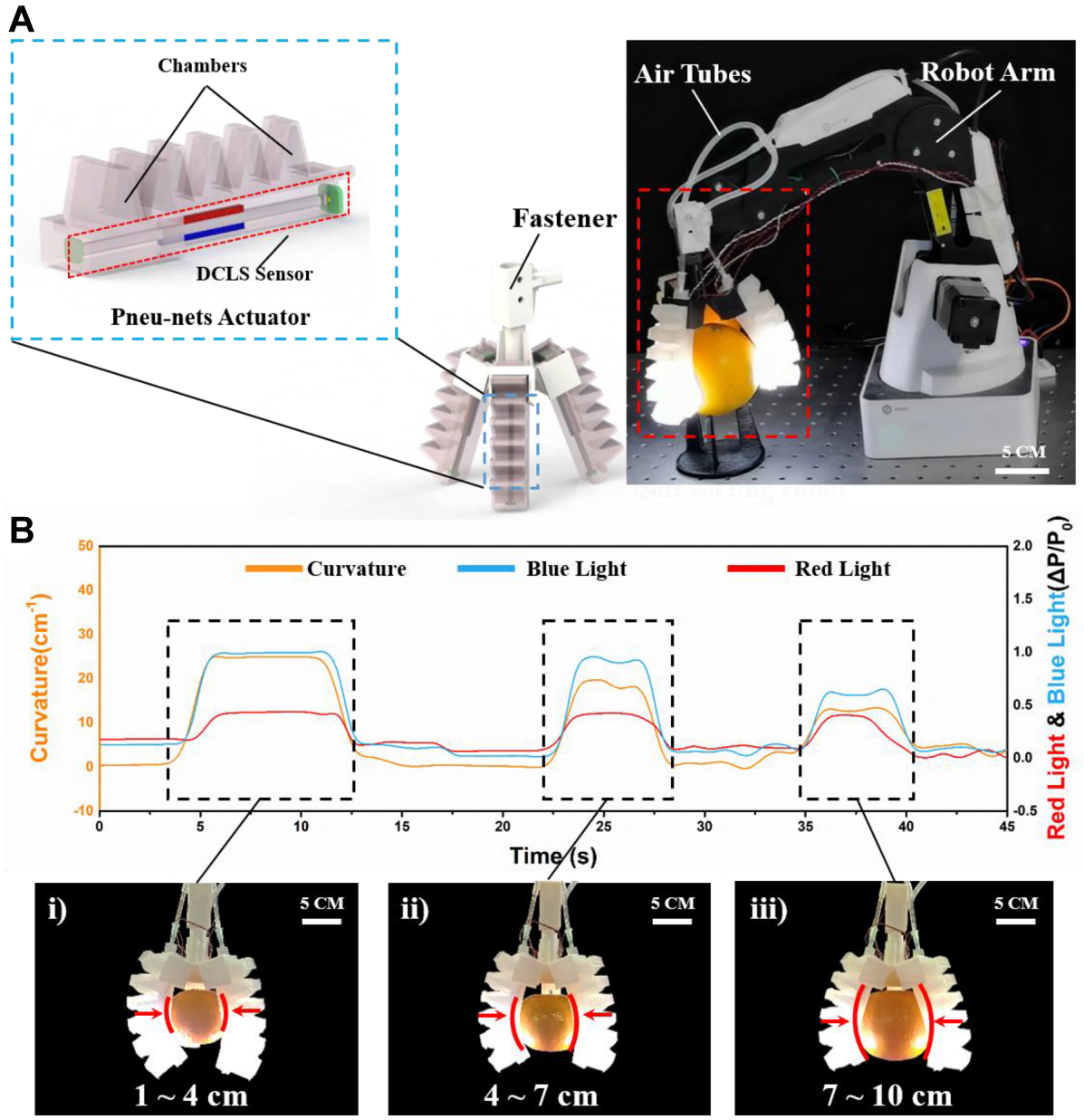

Figure 4. The DCLS sensor application in a fruit sorting robot. (A) Design of the pneu-nets actuator; (B) Sorting tests of the pneu-nets actuator to grasp tangerines with different diameters. DCLS: Dual-colored layer structured.

motor, and microcontroller units. The swinging motion of the robot was meticulously regulated via tendons linking with the servo. Notably, the DCLS sensor eliminates the need for recalibration to detect the tail's swing angle and direction. Figure 5B-D illustrates graphical depictions of the output signals and swing angle of the fish-inspired robot at various frequencies and swing amplitudes, specifically at 30° and 2 Hz [Figure 5B], 45° and 0.7 Hz [Figure 5C], 60° and 0.7 Hz [Figure 5D] [Supplementary Movie 5].

The soft hand orthotic exoskeleton robot, fabricated from elastomeric materials and actuated through air pressure, demonstrates considerable promise for applications encompassing both rehabilitation and gripping assistance[45]. To achieve these objectives, the control strategy relies on employing sensory feedback

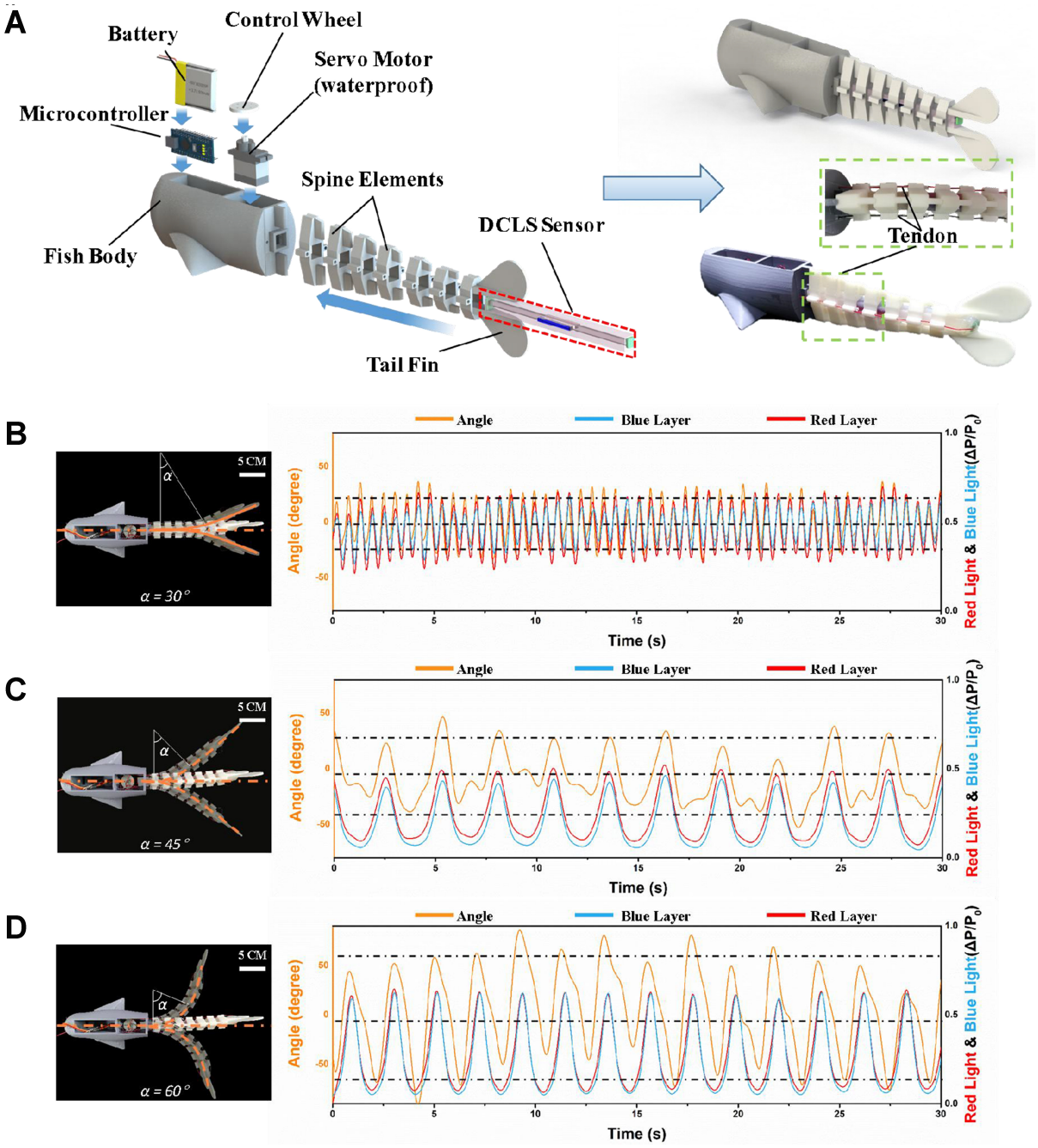

Figure 5. The DCLS sensor application in a fish-inspired robot. (A) Design of the fish-inspired robot; Swinging angles of the fish robot at (B) 30° and 2 Hz, (C) 45° and 0.7 Hz, (D) 60° and 0.7 Hz. DCLS: Dual-colored layer structured.

modalities such as bending angle or position. The details of the design and fabrication can be found in Supplementary Text 6. This enables precise execution of intended motions and facilitates evaluation of recovery progress. The system architecture of the exoskeleton robot is depicted in Figure 6A. The pneu-nets actuator is designed in the same way as the soft sorting robot. Five pneu-nets actuators are used and oriented in a palm-like distribution. To substantiate the sensor's calibration-free capacity, an experiment was conducted by inflating four pneu-nets actuators to achieve predetermined flexion angles. Figure 6B demonstrates consistent bending angles across the four fingers, excluding the thumb. Notably, when placed

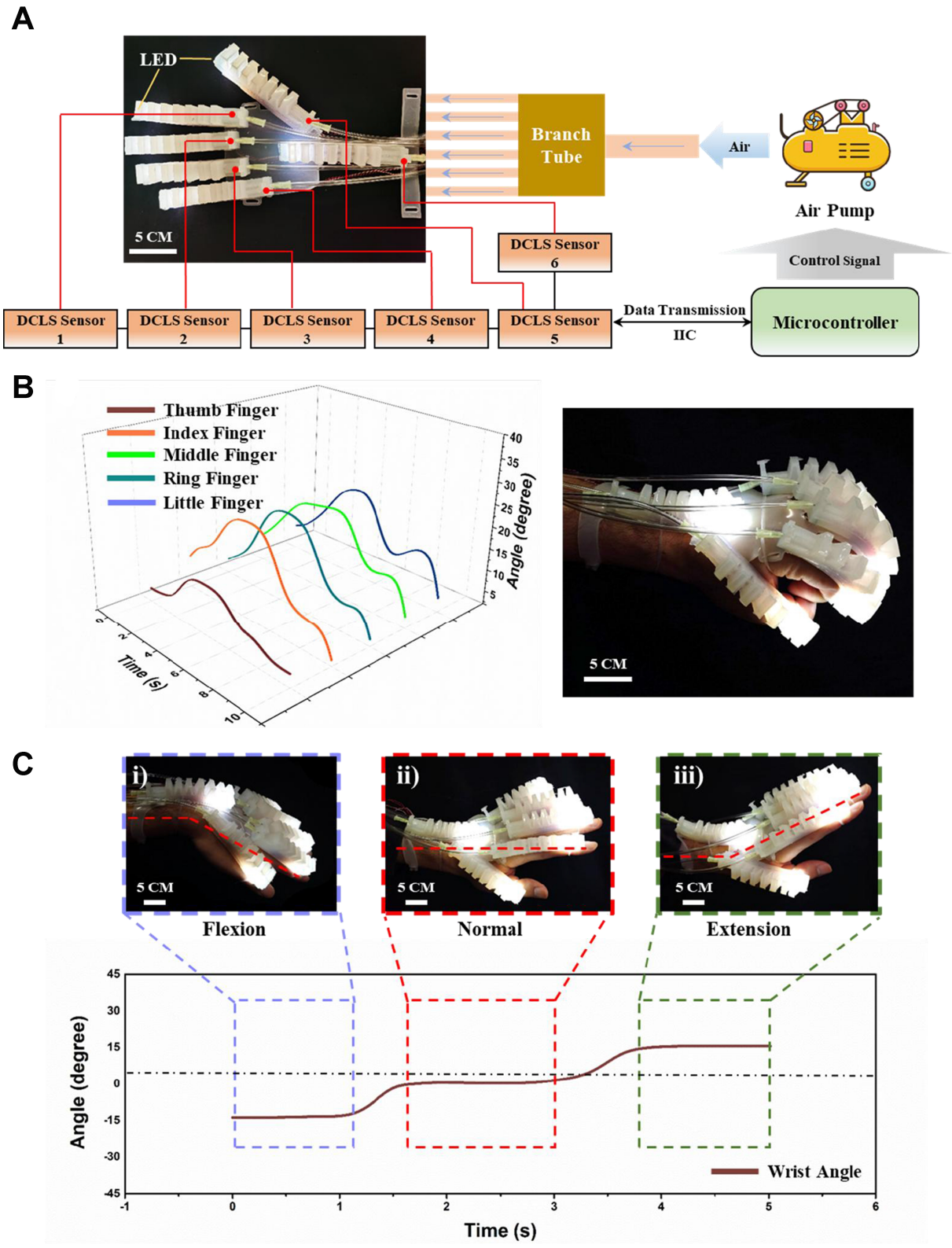

Figure 6. The DCLS sensor application in a hand orthotic exoskeleton robot. (A) System architecture of soft hand orthotic exoskeleton robot; (B) Adaptive detection of bending angles under different bending radii of fingers; (C) Detection of wrist bending directions. DCLS: Dual-colored layer structured.

on surfaces with joints of different sizes, other sensors of the same type must be calibrated to perform the same task. Compared to existing soft bending sensors, the DCLS sensor can be used directly without calibration to accurately sense the bending angle. To validate the directional sensing calibration-free capability of the sensor in the hand orthotic exoskeleton robot, we conducted an experiment involving the actuation of the wrist joint. After a volunteer wore the hand orthotic exoskeleton robot, the wrist actuator assisted in both flexion and extension motions of the wrist joint. Without requiring calibration, the DCLS sensor demonstrated the ability to discern bending direction variations, as depicted in Figure 6C. Additionally, the signal stability of the sensor during routine use is also particularly important. We have determined the variance for each sensor's signal under these two scenarios (handshaking and knocking) by analyzing the temporal data provided by the sensors [Supplementary Table 3 and Supplementary Movie 6]. Notably, the findings indicate that, for both cases, the variance measures for signals of all sensors are below 0.5. This outcome substantiates the robustness of the DCLS sensor within hand orthotic exoskeleton robotics.

CONCLUSIONS

In summary, a novel DCLS bending sensor based on an optical waveguide is proposed and investigated in this paper. The DCLS sensor can directly sense the bending angles and directions of robot joints of different sizes without the need of recalibration. It exhibits good measurement accuracy, resolution, and repeatability. Its sensing capabilities underscore its potential for integration into soft robotics. To showcase its calibration-free characteristic, we engineered three distinct soft robots catering to diverse applications. For the soft sorting robot embedded with the DCLS sensor, the sensor can directly measure the bending curvature of the pneu-nets actuator without calibration, achieving automatic fruit sorting. Furthermore, we have also successfully integrated this sensor into a fish-inspired robot and a hand orthotic exoskeleton robot. The results collectively demonstrate the calibration-free characteristic of the sensor's capability to measure bending angles and directions. We anticipate numerous promising applications for the DCLS sensor in various fields, including but not limited to human-machine interactions, clawing robotics, and human motion monitoring.

DECLARATIONS

Authors' contributions

Writing - original draft: Zhong, L., Peng, Y.
Methodology: Zhong, L., Tian, X., Wang, J. Y., Wang, J. X., Nei, Z., Chen, X.
Supervision and funding acquisition: Peng, Y.
Writing - review and editing: Peng, Y.
All authors reviewed and commented on the manuscript before publication.

Availability of data and materials

The data presented in this study are available upon request from the corresponding author.

Financial support and sponsorship

This research was supported by the National Natural Science Foundation of China (No. 52105563, No. 52475573), the Natural Science Foundation of Zhejiang Province (No. LTGY23E050002), the National Key Research and Development Program of China (No. 2023YFC2811500), Zhijiang Youth Project of Zhejiang Provincial Philosophy and Social Science Planning (No. 22ZJQN14YB), the Key Research and Development Programme of Zhejiang (No. 2023C03196, No. 2022C03103, and No. 2024C03259), and the Fundamental Research Funds for the Central Universities.

Conflicts of interest

All authors declared that there are no conflicts of interest.

Ethical approval and consent to participate

The study protocol was approved by the Medical Ethics Committee from the Department of Psychology and Behavioral Sciences, Zhejiang University, China (reference number: [2022]098), and informed consent was obtained from all participants.

Consent for publication

Not applicable.

Copyright

REFERENCES

1. Wang, Z.; Or, K.; Hirai, S. A dual-mode soft gripper for food packaging. *Robot. Auton. Syst.* **2020**, *125*, 103427. DOI
2. Sinatra, N. R.; Teeple, C. B.; Vogt, D. M.; Parker, K. K.; Gruber, D. F.; Wood, R. J. Ultragentle manipulation of delicate structures using a soft robotic gripper. *Sci. Robot.* **2019**, *4*, eaax5425. DOI PubMed
3. Liu, X.; Song, M.; Fang, Y.; Zhao, Y.; Cao, C. Worm-inspired soft robots enable adaptable pipeline and tunnel inspection. *Adv. Intell. Syst.* **2022**, *4*, 2100128. DOI
4. Tang, Z. Q.; Heung, H. L.; Shi, X. Q.; Tong, R. K. Y.; Li, Z. Probabilistic model-based learning control of a soft pneumatic glove for hand rehabilitation. *IEEE. Trans. Biomed. Eng.* **2022**, *69*, 1016-28. DOI PubMed
5. Runciman, M.; Darzi, A.; Mylonas, G. P. Soft robotics in minimally invasive surgery. *Soft. Robot.* **2019**, *6*, 423-43. DOI PubMed PMC
6. Jin, H.; Dong, E.; Alici, G.; et al. A starfish robot based on soft and smart modular structure (SMS) actuated by SMA wires. *Bioinspir. Biomim.* **2016**, *11*, 056012. DOI
7. Wang, H.; Zhang, R.; Chen, W.; Liang, X.; Pfeifer, R. Shape detection algorithm for soft manipulator based on fiber bragg gratings. *IEEE/ASME. Trans. Mechatron.* **2016**, *21*, 2977-82. DOI
8. Fei, Y.; Wang, J.; Pang, W. A novel fabric-based versatile and stiffness-tunable soft gripper integrating soft pneumatic fingers and wrist. *Soft. Robot.* **2019**, *6*, 1-20. DOI
9. Park, Y. L.; Chau, K.; Black, R. J.; Cutkosky, M. R. Force sensing robot fingers using embedded fiber Bragg grating sensors and shape deposition manufacturing. In: Proceedings 2007 IEEE International Conference on Robotics and Automation; 2007 Apr 10-14; Rome, Italy. IEEE; 2017. pp. 1510-6. DOI
10. Liu, Z.; Wang, Y.; Fei, Y. Soft pipe-climbing robot for vertical creeping locomotion. In: 2021 27th International Conference on Mechatronics and Machine Vision in Practice (M2VIP); 2021 Nov 26-28; Shanghai, China. IEEE; 2021. pp. 316-21. DOI
11. Zhou, P.; Yao, J.; Zhang, X.; Zhao, Y. Design and analysis of a muti-degree-of-freedom dexterous gripper with variable stiffness. In: Intelligent Robotics and Applications: 14th International Conference (ICIRA 2021). Spriger, Cham; 2021. pp. 129-39. DOI
12. Zhang, F.; Jin, T.; Xue, Z.; Zhang, Y. Recent progress in three-dimensional flexible physical sensors. *Int. J. Smart. Nano. Mater.* **2022**, *13*, 17-41. DOI
13. Liu, J.; Liao, F.; Chen, Z.; et al. Digitizing human motion via bending sensors toward humanoid robot. *Adv. Intell. Syst.* **2023**, *5*, 2200337. DOI
14. Ta, T. D.; Umedachi, T.; Kawahara, Y. Inkjet printable actuators and sensors for soft-bodied crawling robots. In: 2019 International Conference on Robotics and Automation (ICRA); 2019 May 20-24; Montreal, Canada. IEEE; 2019. pp. 3658-64. DOI
15. Song, Z.; Matsuda, R.; Matsubara, K.; Nakamura, F.; Ota, H. A caterpillar-inspired soft robot based on thermal expansion. In: 2020 IEEE 33rd International Conference on Micro Electro Mechanical Systems (MEMS); 2020 Jan 18-22; Vancouver, Canada. IEEE; 2020. pp. 489-92. DOI
16. Ge, Q.; Zhou, T.; Gong, T.; Liang, Y.; Augustine, N. L.; Chen, M. Highly sensitive measurement of finger joint angle based on a double-U tapered POF embedded in PDMS film. *Opt. Fiber. Technol.* **2023**, *76*, 103236. DOI
17. Jin, G.; Sun, Y.; Geng, J.; et al. Bioinspired soft caterpillar robot with ultra-stretchable bionic sensors based on functional liquid metal. *Nano. Energy.* **2021**, *84*, 105896. DOI
18. Vogt, D. M.; Wood, R. J. Wrist angle measurements using soft sensors. In: IEEE SENSORS 2014 Proceedings (SENSORS); 2014 Nov 02-05; Valencia, Spain. IEEE; 2014. pp. 1631-4. DOI
19. Wu, P.; Yiu, C. K.; Huang, X.; et al. Liquid metal-based strain-sensing glove for human-machine interaction. *Soft. Sci.* **2023**, *3*, 35. DOI
20. Shu, J.; Wang, J.; Su, Y.; Liu, H.; Li, Z.; Tong, R. K. An end-to-end posture perception method for soft bending actuators based on kirigami-inspired piezoresistive sensors. In: 2022 IEEE-EMBS International Conference on Wearable and Implantable Body Sensor

Networks (BSN); 2022 Sep 27-30; Ioannina, Greece. IEEE; 2022. pp. 1-5. DOI

21. Lee, D. H.; Yang, J. C.; Sim, J. Y.; Kang, H.; Kim, H. R.; Park, S. Bending sensor based on controlled microcracking regions for application toward wearable electronics and robotics. *ACS. Appl. Mater. Interfaces.* **2022**, *14*, 31312-20. DOI
22. Jan, A. A.; Kim, S.; Kim, S. A skin-wearable and self-powered laminated pressure sensor based on triboelectric nanogenerator for monitoring human motion. *Soft. Sci.* **2024**, *4*, 10. DOI
23. Gao, Z.; Ren, B.; Fang, Z.; Kang, H.; Han, J.; Li, J. Accurate recognition of object contour based on flexible piezoelectric and piezoresistive dual mode strain sensors. *Sens. Actuators. A. Phys.* **2021**, *332*, 113121. DOI
24. Chillara, V. S. C.; Ramanathan, A. K.; Dapino, M. J. Self-sensing piezoelectric bistable laminates for morphing structures. *Smart. Mater. Struct.* **2020**, *29*, 085008. DOI
25. Guess, M.; Soltis, I.; Rigo, B.; et al. Wireless batteryless soft sensors for ambulatory cardiovascular health monitoring. *Soft. Sci.* **2023**, *3*, 24. DOI
26. Peng, Y.; Wang, J.; Tian, X.; Liu, T.; Geng, W.; Zhu, Z. An electronic skin strain sensor for adaptive angle calculation. *IEEE. Sensors. J.* **2022**, *22*, 12629-36. DOI
27. Huang, T.; He, P.; Wang, R.; et al. Porous fibers composed of polymer nanoball decorated graphene for wearable and highly sensitive strain sensors. *Adv. Funct. Mater.* **2019**, *29*, 1903732. DOI
28. Wang, X.; Qiu, Y.; Cao, W.; Hu, P. Highly stretchable and conductive core–sheath chemical vapor deposition graphene fibers and their applications in safe strain sensors. *Chem. Mater.* **2015**, *27*, 6969-75. DOI
29. Wang, R.; Jiang, N.; Su, J.; et al. A Bi-sheath fiber sensor for giant tensile and torsional displacements. *Adv. Funct. Mater.* **2017**, *27*, 1702134. DOI
30. To, C.; Hellebrekers, T.; Jung, J.; Yoon, S. J.; Park, Y. A soft optical waveguide coupled with fiber optics for dynamic pressure and strain sensing. *IEEE. Robot. Autom. Lett.* **2018**, *3*, 3821-7. DOI
31. Wu, C.; Liu, X.; Ying, Y. Soft and stretchable optical waveguide: light delivery and manipulation at complex biointerfaces creating unique windows for on-body sensing. *ACS. Sens.* **2021**, *6*, 1446-60. DOI
32. Zhao, H.; O'Brien, K.; Li, S.; Shepherd, R. F. Optoelectronically innervated soft prosthetic hand via stretchable optical waveguides. *Sci. Robot.* **2016**, *1*, eaai7529. DOI PubMed
33. Krauss, H.; Takemura, K. Stretchable optical waveguide sensor capable of two-degree-of-freedom strain sensing mediated by a semidivided optical core. *IEEE/ASME. Trans. Mechatron.* **2022**, *27*, 2151-7. DOI
34. Chen, W.; Xiong, C.; Liu, C.; Li, P.; Chen, Y. Fabrication and dynamic modeling of bidirectional bending soft actuator integrated with optical waveguide curvature sensor. *Soft. Robot.* **2019**, *6*, 495-506. DOI PubMed PMC
35. Kim, T.; Lee, S.; Hong, T.; Shin, G.; Kim, T.; Park, Y. L. Heterogeneous sensing in a multifunctional soft sensor for human-robot interfaces. *Sci. Robot.* **2020**, *5*, eabc6878. DOI
36. Bai, H.; Li, S.; Barreiros, J.; Tu, Y.; Pollock, C. R.; Shepherd, R. F. Stretchable distributed fiber-optic sensors. *Science* **2020**, *370*, 848-52. DOI
37. Liu, X.; Wang, L.; Xiang, Y.; et al. Magnetic soft microfiberbots for robotic embolization. *Sci. Robot.* **2024**, *9*, eadh2479. DOI PubMed
38. Xing, L.; Wang, X.; Li, M.; et al. Self-adhesive, stretchable waterborne polyurethane-based flexible film as wearable conformal strain sensor for motion and health monitoring. *Adv. Nanocompos.* **2024**, *1*, 171-9. DOI
39. Zhao, H.; Jalving, J.; Huang, R.; Knepper, R.; Ruina, A.; Shepherd, R. A helping hand: soft orthosis with integrated optical strain sensors and EMG control. *IEEE. Robot. Automat. Mag.* **2016**, *23*, 55-64. DOI
40. Bryant, F. Snell's law of refraction. *Phys. Bull.* **1958**, 9,317. DOI
41. Gray, G. T.; Maudlin, P. J.; Hull, L. M.; Zuo, Q. K.; Chen, S. Predicting material strength, damage, and fracture *The synergy between experiment and modeling*. *J. Fail. Anal. Preven.* **2005**, *5*, 7-17. DOI
42. Zhang, J.; Lai, S.; Yu, H.; et al. Fruit classification utilizing a robotic gripper with integrated sensors and adaptive grasping. *Math. Probl. Eng.* **2021**, *2021*, 1-15. DOI
43. Liu, S.; Wang, Y.; Li, Z.; Jin, M.; Ren, L.; Liu, C. A fluid-driven soft robotic fish inspired by fish muscle architecture. *Bioinspir. Biomim.* **2022**, *17*, 026009. DOI
44. Li, G.; Chen, X.; Zhou, F.; et al. Self-powered soft robot in the Mariana Trench. *Nature* **2021**, *591*, 66-71. DOI
45. Li, M.; He, B.; Liang, Z.; et al. An attention-controlled hand exoskeleton for the rehabilitation of finger extension and flexion using a rigid-soft combined mechanism. *Front. Neurorobot.* **2019**, *13*, 34. DOI PubMed PMC